Design of SARS-CoV-2 papain-like protease inhibitor with antiviral efficacy in a mouse model

Bin Tan[1*], Xiaoming Zhang[2*], Ahmadullah Ansari[3,4*], Prakash Jadhav[1*], Haozhou Tan[1], Kan Li[1], Ashima Chopra[3,4], Alexandra Ford[5], Xiang Chi[2], Francesc Xavier Ruiz[3,4]†, Eddy Arnold[3,4]†, Xufang Deng[2,6]†, Jun Wang[1]†

[1]Department of Medicinal Chemistry, Ernest Mario School of Pharmacy, Rutgers, the State University of New Jersey, Piscataway, NJ, 08854, USA

[2]Department Physiological Sciences, College of Veterinary Medicine, Oklahoma State University, Stillwater, OK, 74078, USA

[3]Center for Advanced Biotechnology and Medicine, Rutgers, the State University of New Jersey, Piscataway, NJ, 08854, USA

[4]Department of Chemistry and Chemical Biology, Rutgers, the State University of New Jersey, Piscataway, NJ, 08854, USA

[5]Deprtment of Veterinary Pathobiology, College of Veterinary Medicine, Oklahoma State University, Stillwater, OK, 74078, USA

[6]Oklahoma Center for Respiratory and Infectious Diseases, Oklahoma State University, Stillwater, OK, 74078, USA

[*]These authors contributed equally to this work

†Corresponding author. Email: junwang@pharmacy.rutgers.edu (J.W.); xufang.deng@okstate.edu (X.D.); arnold@cabm.rutgers.edu (E.A.); xavier@cabm.rutgers.edu (F.X.R.)

Abstract: The emergence of SARS-CoV-2 variants and drug-resistant mutants calls for additional oral antivirals. The SARS-CoV-2 papain-like protease (PL^{pro}) is a promising but challenging drug target. In this study, we designed and synthesized 85 noncovalent PL^{pro} inhibitors that bind to the newly discovered $Val70^{Ub}$ site and the known BL2 groove pocket. Potent compounds inhibited PL^{pro} with inhibitory constant K_i values from 13.2 to 88.2 nM. The co-crystal structures of PL^{pro} with eight leads revealed their interaction modes. The *in vivo* lead **Jun12682** inhibited SARS-CoV-2 and its variants, including nirmatrelvir-resistant strains with EC_{50} from 0.44 to 2.02 μM. Oral treatment with **Jun12682** significantly improved survival and reduced lung viral loads and lesions in a SARS-CoV-2 infection mouse model, suggesting PL^{pro} inhibitors are promising oral SARS-CoV-2 antiviral candidates.

One-Sentence Summary: Structure-guided design of SARS-CoV-2 PL^{pro} inhibitors with *in vivo* antiviral efficacy in a mouse model.

The COVID-19 pandemic is a timely call for the urgent need for orally bioavailable antivirals. The FDA has approved three direct-acting antivirals, including two viral RNA-dependent RNA polymerase inhibitors, remdesivir and molnupiravir, and one viral main protease (M^{pro}) inhibitor, nirmatrelvir (*1*). Remdesivir is administered by intravenous injection, and its use is limited to hospitalized patients. The clinical efficacy of remdesivir is also controversial (*2*). Molnupiravir is a mutagen and should not be used in pregnant women (*3*). Nirmatrelvir is co-administered with ritonavir, a CYP3A4 inhibitor, to improve the *in vivo* half-life (*4*). For this reason, Paxlovid, a combination of nirmatrelvir and ritonavir, has drug-drug interaction concerns. Ensiltrelvir is a second-generation M^{pro} inhibitor approved in Japan (*5*). Although it is highly efficacious in clinical trials (*6*), ensitrelvir is a potent CYP3A4 inhibitor that may lead to severe adverse drug-drug interactions with other medications (*7, 8*). Mutant SARS-CoV-2 viruses with resistance against remdesivir or nirmatrelvir have been identified from viral passage experiments in cell culture (*9-11*) and drug-treated COVID-19 patients (*12-15*). Therefore, additional antivirals with alternative mechanisms of action are urgently needed to combat drug-resistant and emerging SARS-CoV-2 variants.

The papain-like protease (PL^{pro}) is one of the two viral cysteine proteases encoded by SARS-CoV-2. PL^{pro} cleaves the viral non-structural (nsp) polyproteins at the nsp1/2, nsp2/3, and nsp3/4 junctions and is pivotal for viral replication (*16*). In addition, PL^{pro} suppresses the host immune response through cleaving ubiquitin and interferon-stimulated gene 15 (ISG-15) modifications from host proteins (*17-19*). The SARS-CoV-2 PL^{pro} sequence is 82.9% identical to SARS-CoV-1 PL^{pro}. PL^{pro} is highly conserved among SARS-CoV-2 variants (*20*), rendering it a high-profile antiviral drug target (*19, 21*). However, despite decades of medicinal chemistry optimization and high-throughput screening, no drug-like PL^{pro} inhibitor has shown *in vivo* antiviral efficacy in SARS-CoV-2-infected animal models (*20*). PL^{pro} substrates contain a consensus motif LXGG↓(N/K/X) (*16*). The S1 and S2 subsites of PL^{pro} form a narrow tunnel for binding two glycines (*22*). The absence of binding pockets near the catalytic cysteine Cys111 presents a challenge in designing highly potent PL^{pro} inhibitors. In this study, we describe the design of potent PL^{pro} inhibitors by exploiting a novel drug-binding site that accommodates the ubiquitin Val70 side chain ($Val70^{Ub}$). We validate PL^{pro} as a viable drug target by demonstrating the *in vivo* antiviral efficacy of a designed PL^{pro} inhibitor **Jun12682** with oral administration in SARS-CoV-2 infected mice.

Discovery of the binding site for ubiquitin Val70 as a new drug binding site on PL^{pro}

Before our study, noncovalent and covalent PL^{pro} inhibitors were reported (*20, 23*). One potent noncovalent PL^{pro} inhibitor is **XR8-24**, which has an IC_{50} of 0.56 μM in the fluorescence resonance energy transfer (FRET) enzymatic assay and an EC_{50} of 1.2 μM in the antiviral assay (*24*). Compound 7 (**Cp7**) is a rationally designed covalent PL^{pro} inhibitor with a fumarate reactive warhead that inhibits PL^{pro} with an IC_{50} of 0.094 μM and SARS-CoV-2 replication with an EC_{50} of 1.1 μM (*25*). Inspired by these results, we designed a hybrid covalent PL^{pro} inhibitor **Jun11313** by converting the naphthalene in **Cp7** to 3-phenylthiophene (Fig. 1A); **Jun11313** potently inhibited PL^{pro} with an IC_{50} of 0.12 μM.

The lead covalent compound **Jun11313** was co-crystallized with SARS-CoV-2 PL^{pro} to visualize the key interactions for binding. We determined the co-crystal structure at 2.85 Å resolution (PDB: 8UVM). As expected, the fumarate ester electrophile forms a covalent bond with the catalytic Cys111 (Fig. 1B). **Jun11313** forms hydrogen bonds with main-chain atoms of Leu162, Gly163, Tyr268, and Gly271, as well as with side-chain atoms of Trp106 and His272.

Jun11313 also makes extensive van der Waals contacts with Leu162, Tyr264, Pro247, Pro248, and Thr301 (Fig. 1B).

Surprisingly, the thienyl group in **Jun11313** is oriented towards the opposite side of the BL2 groove compared to the pyrrolidine-substituted thienyl group in **XR8-24** (Fig. 1C). The phenylthiophene in **XR8-24** makes extensive contacts with the BL2 groove, namely van der Waals interactions with residues surrounding the cavity (Pro248, Tyr264, and Tyr268; Fig. 1C). In comparison, the phenylthienyl group of **Jun11313** is oriented towards Pro247, making van der Waals contacts with both Pro248 and Pro247, and CH–π and S–π interactions with Met208 (Fig. 1B). While the strength of these interactions is difficult to estimate and has been understudied in drug design (*26, 27*), here they may be the culprit for **Jun11313**'s unexpected conformation (Fig. 1B). If the methyl pyrrolidine group in **XR8-24** were arranged as the phenylthienyl group of **Jun11313**, it should orient in a very solvent-exposed region to avoid a clash with Met208 (fig. S1A).

Superimposition of PL^{pro} structures complexed with ubiquitin and **Jun11313** revealed that the thienyl group occupies the same hydrophobic site as Val70 from ubiquitin (Fig. 1D). Therefore, we designate this pocket as the $Val70^{Ub}$ site. The comparison of the co-crystal structures of PL^{pro} with **Jun11313** and with ubiquitin suggests that this site is essential for binding both the ubiquitin substrate and this inhibitor. Similarly, the superimposition of PL^{pro} structures complexed with ISG15 showed that the thienyl group interacts with the analogous Asn151-Leu152 site from ISG15 (fig. S1B).

Rational design of biarylphenyl PL^{pro} inhibitors

The unexpected binding pose of **Jun11313** in PL^{pro} led us to hypothesize that potent PL^{pro} inhibitors can be designed by simultaneously engaging the BL2 groove pocket and the $Val70^{Ub}$ hydrophobic site (Fig. 1E). It is noteworthy that the $Val70^{Ub}$ site has not been explored for PL^{pro} inhibitor design (*20*). We designed and synthesized a library of 85 biarylphenyl benzamide compounds (Fig. S2). Aryl substitutions were installed on the 3 and 5 positions of the phenylethylamine ring to engage hydrophobic interactions with residues in the BL2 groove and the ubiquitin $Val70^{Ub}$ binding site (Fig. 1E). In addition, diverse amines were installed on the meta-position of the benzoic acid to engage electrostatic interactions with Glu167 (*24*). The central 1-phenylethyl benzamide core structure was kept intact to maintain the critical hydrogen bonds and π-π interactions with the BL2 loop. All synthesized compounds were initially tested in the FRET-based enzymatic assay and the cytotoxicity assay in Vero E6 cells (Fig. 1F). Promising lead compounds were then tested in a secondary FlipGFP PL^{pro} assay and SARS-CoV-2 antiviral assay (*28*). FlipGFP PL^{pro} is a cell-based assay that validates intracellular PL^{pro} target engagement (*22*). Next, leads were profiled for *in vitro* microsomal stability and *in vivo* oral pharmacokinetic (PK) properties in mice. **Jun12682** was finalized as the *in vivo* lead for the SARS-CoV-2 infection mouse model study.

A complete list of the designed biarylphenyl PL^{pro} inhibitors is shown in fig. S2, with representative examples in Table 1. Among the 85 compounds tested in the FRET assay, 26 had IC_{50} < 100 nM, 42 had IC_{50} between 100 – 200 nM, and 14 had IC_{50} between 200 – 400 nM. The control compound **GRL0617** had IC_{50} values of 1.92 μM. The inhibitory constant K_i was determined for potent compounds (Table 1). The first designed compound, **Jun11875,** inhibited PL^{pro} with a K_i of 13.2 nM, a 104-fold improvement over **GRL0617** (K_i = 1,374 nM). However, thiophene-containing compounds were generally cytotoxic in Vero E6 cells (CC_{50} < 20 μM). Next, we examined several symmetric and asymmetric five and six-membered aromatic

substitutions at the 3 and 5-positions to mitigate cellular cytotoxicity while maintaining enzymatic inhibition. Among the list of heterocycle substitutions examined, pyrazole was shown to confer potent PL^{pro} inhibition and reduced cellular cytotoxicity. It is noted that despite the potent PL^{pro} enzymatic inhibition for **Jun1247** (IC_{50} = 165.3 nM), **Jun121210** (IC_{50} = 81.9 nM), **Jun121911** (IC_{50} = 73.2 nM), **Jun12208** (IC_{50} = 91.6 nM), and **Jun12242** (IC_{50} = 90.5 nM), their cellular activities were moderate to weak as shown by the FlipGFP assay (EC_{50} > 10 μM) (fig. S2), which might due to poor membrane permeability. The most potent compounds **Jun12199** and **Jun12197** had EC_{50} of 0.8 and 0.6 μM, respectively, more than 20-fold improved from **GRL0617** (EC_{50} = 22.4 μM). The *in vivo* lead **Jun12682** inhibited PL^{pro} with a K_i of 37.7 nM and displayed an EC_{50} of 1.1 μM in the FlipGFP PL^{pro} assay.

Prioritized lead compounds were tested in the SARS-CoV-2 antiviral assay and had EC_{50} from 0.23 to 1.15 μM. **Jun12682** had EC_{50} values of 0.42 and 0.51 μM in the icSARS-CoV-2-nLuc reporter virus and plaque assays, respectively (fig. S3). To examine the potential of PL^{pro} inhibitors in inhibiting SARS-CoV-2 variants and drug-resistant mutants, we selected two PL^{pro} inhibitors **Jun11941** and **Jun12682** to test against SARS-CoV-2 delta and omicron variants and three recombinant SARS-CoV-2 viruses that are resistant to nirmatrelvir, rNsp5-S144M, rNsp5-L50F/E166V, and rNsp5-L50F/E166V/L167F (Fig. 2, A to C). S144M and E166V are nirmatrelvir-resistant mutations identified from enzymatic assays and viral passage experiments (*9, 10*). **Jun11941** and **Jun12682** showed consistent antiviral activity against these viruses with EC_{50} fold-increases less than 1.5 and 2.0, respectively, compared to wild-type (WT). In comparison, the rNsp5-S144M, rNsp5-L50F/E166V, and rNsp5-L50F/E166V/L167F showed significant resistance to nirmatrelvir with EC_{50} fold-increases of 12.5, 24.2, and 21.7, respectively, compared to WT.

Mechanism of action of Jun12682 in inhibiting SARS-CoV-2 PL^{pro}

PL^{pro} is known to antagonize the host innate immune response upon viral infection by hydrolyzing the isopeptide bond between ubiquitin and ISG-15 to lysine side chains of host proteins (*17, 18*). To characterize whether **Jun12682** inhibits the deubiquitinating and deISGylating activities of SARS-CoV-2 PL^{pro}, we performed the PL^{pro} enzymatic assay using Ub-AMC and ISG15-AMC substrates (*22*). **Jun12682** showed potent enzymatic inhibition with K_i values of 63.5 and 38.5 nM in the ubiquitin-AMC (7-amino-4-methylcoumarin) and ISG15-AMC FRET assays (Fig. 2, D to G). The results are consistent with **GRL0617** and **XR8-24** *(22, 24)*. To profile the off-target effect, **Jun12682** was tested against two closest human structural homologs of PL^{pro}, USP7, and USP14 (*24, 29*). **Jun12682** displayed no inhibition of USP7 and USP14-catalyzed Ub-AMC hydrolysis at up to 40 μM (Fig. 2, H and I). **Jun12682** also showed dose-dependent stabilization of SARS-CoV-2 PL^{pro} and was more potent than GRL0617 in the differential scanning fluorimetry assay (Fig. 2J).

X-ray crystal structures of SARS-CoV-2 PL^{pro} with inhibitors

The X-ray co-crystal structures of SARS-CoV-2 PL^{pro} were solved for eight biarylphenyl PL^{pro} inhibitors, **Jun11941**, **Jun12129**, **Jun12303**, **Jun12162**, **Jun12199**, **Jun12197**, **Jun12145**, and **Jun12682** (resolution range of 2.5-3.1 Å, Fig. 3, table S1). The phenylthienyl group of **Jun11313** binds to the $Val70^{Ub}$ site of SARS-CoV-2 PL^{pro} in the region where residues $Val70^{Ub}$ and $Leu71^{Ub}$ at the end of a β sheet in ubiquitin interact with PL^{pro} (an analogous situation happens with residues Asn151 and Leu152 of ISG-15, fig. S1B) (Fig. 1B). This is a unique property of **Jun11313** due to the unusual binding conformation of the phenylthienyl group, which we have subsequently exploited in a new compound series (Fig. 3), exemplified by **Jun12682**. The 2.52 Å

resolution co-crystal structure of PL^{pro} with **Jun12682** reveals the "best of both worlds", with the N-ethyl and N-methyl pyrazole substituents in the phenyl moiety binding toward the Met208/Pro247 direction ($Val70^{Ub}$ site) and the Pro248/Tyr264/Tyr268 direction (BL2 groove), respectively (Fig. 3A). While Met208 remains involved in CH–π and S–π interactions with the pyrazole ring, it also displays a van der Waals contact with the methyl substituent. Moreover, the phenyl group of **Jun12682** makes a π–π interaction with the side chain of Tyr264 (Fig. 3A). Fig. 3B-I shows the unbiased electron density of PL^{pro} inhibitors **Jun12145**, **Jun12303**, **Jun12199**, **Jun12162**, **Jun12129**, **Jun12197**, and **Jun11941**, in a similar conformation to **Jun12682**. The disubstituted phenyl group has two alternative conformations in the **Jun12145** and **Jun12129** complex structures, as indicated by the refined electron density (Fig. 3C, G; fig. S4). Despite the differences between compounds, the interactions depicted in Fig. 3A between PL^{pro} and **Jun12682** are conserved in all complexes (fig. S4). The crystallographic data and refinement statistics are listed in table S1.

In vitro and *in vivo* pharmacokinetic (PK) profiling identified Jun12682 as an *in vivo* lead candidate

PL^{pro} inhibitors with potent SARS-CoV-2 antiviral activity ($EC_{50} \leq 1$ μM) and a high selectivity index (SI > 50) were selected for *in vitro* microsomal stability assay and *in vivo* oral PK studies in mice. Most pyrazole-containing PL^{pro} inhibitors showed high stability in the mouse microsomal stability assay ($T_{1/2} > 60$ min) (Table 1). Next, ten compounds were advanced to the *in vivo* oral snap PK in C57BL/6J mice (Fig. 4A, B; table S2). Compounds were dosed to 3 male C57BL/6J mice per group at 50mg/kg through oral gavage, and blood samples were collected at 0.5, 1, 3, and 5 h, and the drug concentration was quantified by LC-MS/MS. **Jun12199** and **Jun12682** showed the highest *in vivo* plasma concentrations. Given the faster absorption of **Jun12682** compared to **Jun12199**, **Jun12682** was selected as an *in vivo* lead candidate. A 24-hour *in vivo* PK study was conducted to determine the oral bioavailability of **Jun12682** (Fig. 4C; table S3). **Jun12682** had a rapid absorption after p.o. administration (50 mg/kg) and reached the maximum plasma concentration at 1.67 h (T_{max}), with a peak plasma concentration (C_{max}) of 4537 ng/mL. The clearance of **Jun12682** was moderate, with a half-life ($t_{1/2}$) of 2.01 h (table S3). The plasma drug concentration was above the antiviral EC_{90} value (1.59 μM) for 7 h. The oral bioavailability of **Jun12682** was 72.8%.

Further profiling of the *in vitro* PK properties revealed that **Jun12682** was highly stable in the human microsomes ($T_{1/2} = 131.9$ min, CLint(mic) = 10.5 μL/min/mg) and had high selectivity for CYP1A2, 2C9, 2C19, 2D6, and 3A-M ($IC_{50} > 50.0$ μM) (Fig. 4D). **Jun12682** had a kinetic solubility of 180 μM and a thermodynamic solubility greater than 5mg/ml. The mouse plasma protein binding was 85.4%. Overall, **Jun12682** showed favorable *in vitro* and *in vivo* PK properties amenable for the *in vivo* antiviral efficacy study.

In vivo antiviral efficacy of Jun12682 in a SARS-CoV-2 infection mouse model

To assess the *in vivo* antiviral efficacy of **Jun12682**, we utilized a lethal SARS-CoV-2 mouse model described in (*30*). This model involves infecting young Balb/c mice (9 to 12 weeks old) with a mouse-adapted $SARS2\text{-}N501Y_{MA30}$, resulting in severe lung disease resembling human patients' lung injuries. This model has been widely used for evaluating SARS-CoV-2 therapeutics and vaccine candidates (*31-34*). To this end, young Balb/c mice were intranasally infected with 5,600 PFUs of $SARS2\text{-}N501Y_{MA30}$ and orally administered **Jun12682** at 500 mg/kg twice daily for 5 days (Fig. 4E). The weight loss plot (Fig. 4F) illustrates that mice

administered with the vehicle experienced rapid body weight loss exceeding 20%, leading to a 100% fatality rate by 5 DPI (day post inoculation) (Fig. 4G). In contrast, most mice treated with **Jun12682** exhibited reduced weight loss, resulting in a significantly improved survival rate (0% vs. 70%, $p < 0.0001$) (n = 10, two independent studies). To further evaluate **Jun12682**'s *in vivo* efficacy, two lower dosages (125, 250 mg/kg) were tested with reduced dosing times from 5 days to 3 days twice daily (Fig. 4H). Mice treated with a dose of 250 mg/kg showed an average of 10% maximum weight loss, providing evident protection from infection compared to the vehicle- and 125 mg/kg-treated groups, which exhibited over 20% weight loss (Fig. 4I). Survival analyses demonstrated that **Jun12682**-treated mice had statistically higher survival rates compared to the vehicle group (0% survival): 125 mg/kg (20%, $p = 0.0428$), and 250 mg/kg (100%, $p < 0.0001$) (Fig. 4J). The three-day treatment of 250 mg/kg dose conferred even better protection than the five-day treatment of 500 mg/kg dose, possibly due to reduced drug toxicity. Lung viral load analyses revealed that at 2 DPI, the vehicle-treated mice had robust infections in the lungs (mean lung titer of $\log_{10}$ 9.17 ± 0.124 PFUs/ml), while the 250 mg/kg **Jun12682**-treated mice had statistically lower lung viral titers (mean lung titers of $\log_{10}$ 8.87 ± 0.194 PFUs/ml, $p = 0.0199$) (Fig. 4K). The antiviral effect of the 250 mg/kg treatment was more evident at 4 DPI with over a log viral titer reduction comparing to the vehicle treatment (mean lung titers of $\log_{10}$ 7.05 ± 0.401 and $\log_{10}$ 5.73 ± 0.528 PFUs/ml for the vehicle and 250 mg/kg groups, respectively, $p = 0.00247$) (Fig. 4K), corroborating the weight loss and survival data (Fig. 4, I and J).

Quantitative PCR analysis of the RNA samples extracted from 2 DPI mice lungs showed that the 250mg/kg treatment significantly reduced the viral N gene level (Fig. 4L) and the expression of multiple inflammatory cytokines, including IFN-β, IL-1β, IL-6, and CXCL10 (*35*) (Fig. 4M). Histopathological analysis revealed that lungs from the vehicle-treated, SARS2-N501Y$_{MA30}$–infected mice at 4 DPI exhibited multifocal pulmonary lesions, including lymphocytic perivascular cuffing, pulmonary edema, hyaline membrane formation, and interstitial thickening and inflammation compared with **Jun12682**-treated mice (Fig. 4N, O; fig. S5). Immunohistochemical analysis using a monoclonal antibody to detect SARS-CoV-2 nucleocapsid (N) in the lungs demonstrated strong and expansive antigen staining in lungs from vehicle-treated, infected mice, whereas **Jun12682** treatment considerably decreased viral antigen staining levels with a few sporadic positive cells (Fig. 4P, Q; fig. S6), consistent with the lung viral titer results (Fig. 4K). Mock-infected lungs were negative for nucleocapsid staining. Overall, the reduced viral replication in the lung and the expression of inflammatory cytokines (Fig. 4K to M) corroborates with the reduced lung inflammation and N protein staining at 4 DPI (Fig. 4N to Q). In summary, these findings demonstrate that oral administration of our rationally designed PL^{pro} inhibitor **Jun12682** efficiently inhibited SARS-CoV-2 replication and mitigated SARS-CoV-2 induced lung lesions *in vivo*, and it represents a promising candidate for further development as orally bioavailable SARS-CoV-2 antivirals. PL^{pro} inhibitors can be used alone or in combination with existing RdRp and M^{pro} inhibitors to combat SARS-CoV-2 variants and drug-resistant mutants.

Acknowledgments: We thank Shannon Cowan and Caden Miller at the Immunopathology Core of the Oklahoma Center for Respiratory and Infectious Diseases for their technical assistance.

Funding:

National Institutes of Health grant U19AI171110 (J.W., E.A.)

National Institutes of Health grant R01AI158775 (J.W., X.D.)

National Institute of Food and Agriculture grants 2023-67015-39096 and 2023-70432-39482 (X.D.)

USDA-ARS Non-Assistance Cooperative Agreement 58-5030-3-047 (X.D.)

Center for Advancement of Science & Technology (OCAST) grant HR23-096 (X.D.)

Author contributions:

J.W., X.D., and E.A. conceived and supervised the research and designed the experiments; J.W., B.T., and P.J. designed the inhibitors; B.T., and P.J. performed chemical syntheses, separation, purification, and structural characterizations; A.A., A.C., and F.X.R. performed gene expression, protein purification, crystallization, and diffraction data collection; A.A., A.C., and F.X.R., and E.A. determined and analyzed the crystal structures; B.T., H.T., and K.L. performed enzymatic inhibition assays, DSF assays, and cellular cytotoxicity assays; X.Z. performed *in vitro* cellular antiviral assays and *in vivo* antiviral studies; A.F. performed the histopathology and immunohistochemistry (IHC) assessment; X.C. performed the mouse tissue analysis and generated the recombinant SARS-CoV-2 viruses; J.W., B.T., X.Z., A.A., A.F., X.C., F.X.R., X.D., and E.A. analyzed and discussed the data with the assistance of P.J., H.T., K.L., and A.C.; and J.W., A.A., F.X.R., E.A., and X.D. wrote the manuscript with the assistance of B.T., X.Z., P.J., H.T., K.L., A.C., and A.F.

Competing interests: Rutgers, the State University of New Jersey, has applied for PCT patents that cover the PL^{pro} inhibitors reported in this manuscript and related compounds.

Data and materials availability: All data are available in the main text or the supplementary materials. The PDB accession numbers for the coordinates of SARS-CoV-2 PL^{pro} in complex with PL^{pro} inhibitors are 8UUW (**Jun12145**), 8UUY (**Jun12129**), 8UUV (**Jun12197**), 8UUU (**Jun12162**), 8UUH (**Jun12199**), 8UUG (**Jun12303**), 8UUF (**Jun11941**), 8UOB (**Jun12682**), and 8UVM (**Jun11313**).

Supplementary Materials

Materials and Methods

Supplementary Text

Figs. S1 to S6

Tables S1 to S3

References (*37–50*)

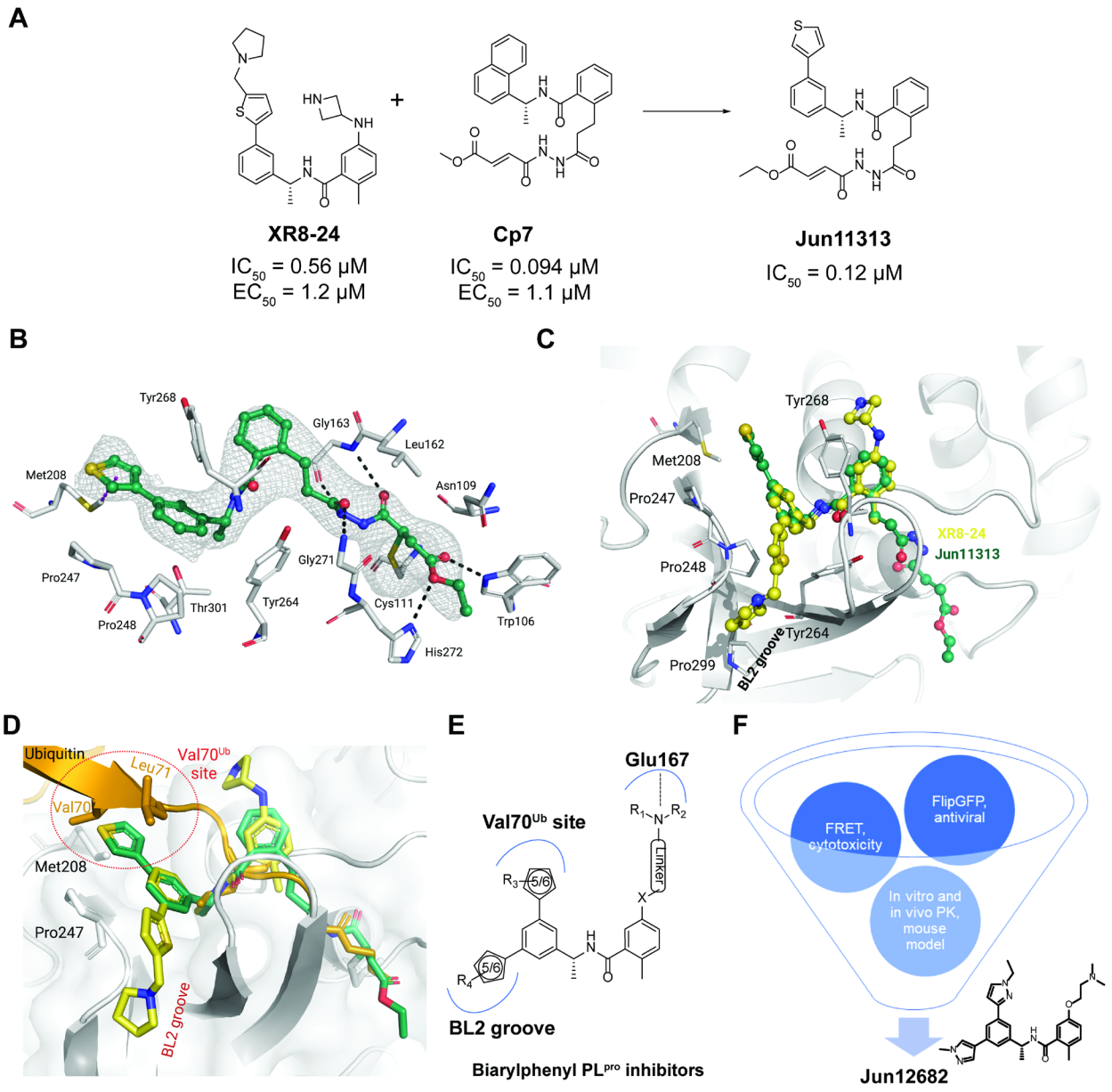

Fig. 1. X-ray crystal structure of the covalent inhibitor Jun11313 with SARS-CoV-2 PL^{pro} and structure-based design of biarylphenyl SARS-CoV-2 PL^{pro} inhibitors. (**A**) Design of the hybrid covalent inhibitor **Jun11313** based on **XR8-24** and **Cp7**. (**B**) Atomic model of the **Jun11313** (in green sticks and spheres) binding site in PL^{pro} (light grey sticks, residues within a 5 Å distance of the inhibitor), with hydrogen bonds displayed as black dashed lines. **Jun11313** polder map (an unbiased difference map (*36*)) is displayed as a grey mesh with 4σ contour. (**C**) Superposition of the PL^{pro}-**Jun11313** structure to the structure of the PL^{pro}-**XR8-24** complex (PDB 7LBS), with **XR8-24** in yellow sticks and spheres, with the relevant residues for binding of both compounds indicated. (**D**) Superimposed X-ray crystal structures of SARS-CoV-2 PL^{pro} with **Jun11313** (green) (PDB: 8UVM), **XR8-24** (yellow) (PDB: 7LBS), and ubiquitin (orange) (PDB: 6XAA). (**E**) Generic chemical structure of the designed biarylphenyl PL^{pro} inhibitor. Critical

interactions are highlighted. (**F**) Flow chart for the lead optimziation of PL^{pro} inhibitors. **Jun12682** was selected as the *in vivo* lead candidate.

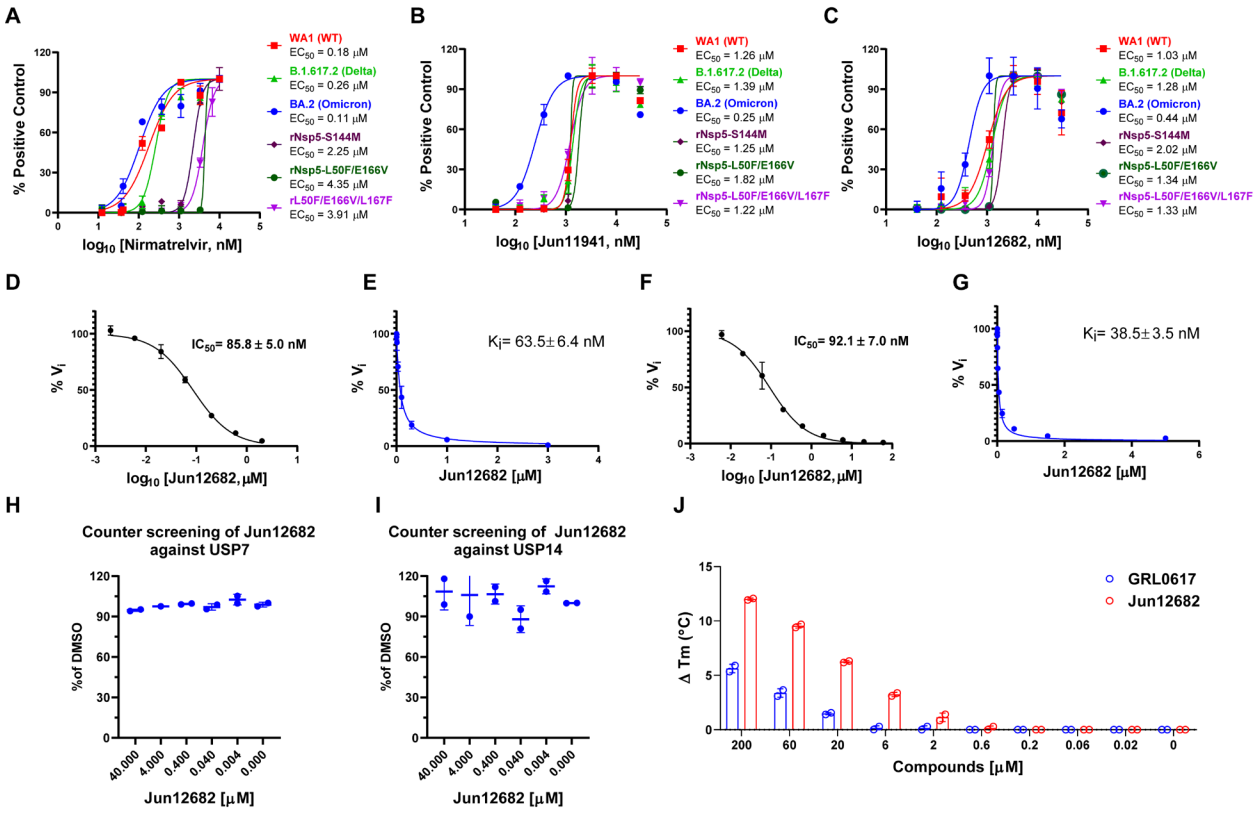

Fig. 2. Antiviral activity of PL^{pro} inhibitors against SARS-CoV-2 variants and mechanistic studies of Jun12682. Antiviral activity of nirmatrelvir (**A**), **Jun11941** (**B**), and **Jun12682** (**C**) against SARS-CoV-2 WA1 strain (WT) (USA-WA1/2020), Omicron strain (BA.2 strain, lineage B.1.1.529, BA.2; HCoV-19/USA/CO-CDPHE-2102544747/2021), Delta strain (Lineage B.1.617.2; hCoV-19/USA/MD-HP05647/2021), and nirmatrelvir-resistant strains rNsp5-S144M, rNsp5-L50F/E166V, and rNsp5-L50F/E166V/L167F. (**D**) IC_{50} curve of **Jun12682** in inhibiting SARS-CoV-2 PL^{pro} hydrolysis of Ub-AMC. (**E**) K_i curve of **Jun12682** in inhibiting SARS-CoV-2 PL^{pro} hydrolysis of Ub-AMC. (**F**) IC_{50} curve of **Jun12682** in inhibiting SARS-CoV-2 PL^{pro} hydrolysis of ISG15-AMC. (**G**) K_i curve of **Jun12682** in inhibiting SARS-CoV-2 PL^{pro} hydrolysis of ISG15-AMC. (**H**) Counter screening of **Jun12682** in inhibiting USP7 hydrolysis of Ub-AMC. (**I**) Counter screening of **Jun12682** in inhibiting USP14 hydrolysis of Ub-AMC. (**J**) Differential scanning fluorimetry assay of **Jun12682** and GRL0617 in stabilizing the SARS-CoV-2 PL^{pro}.

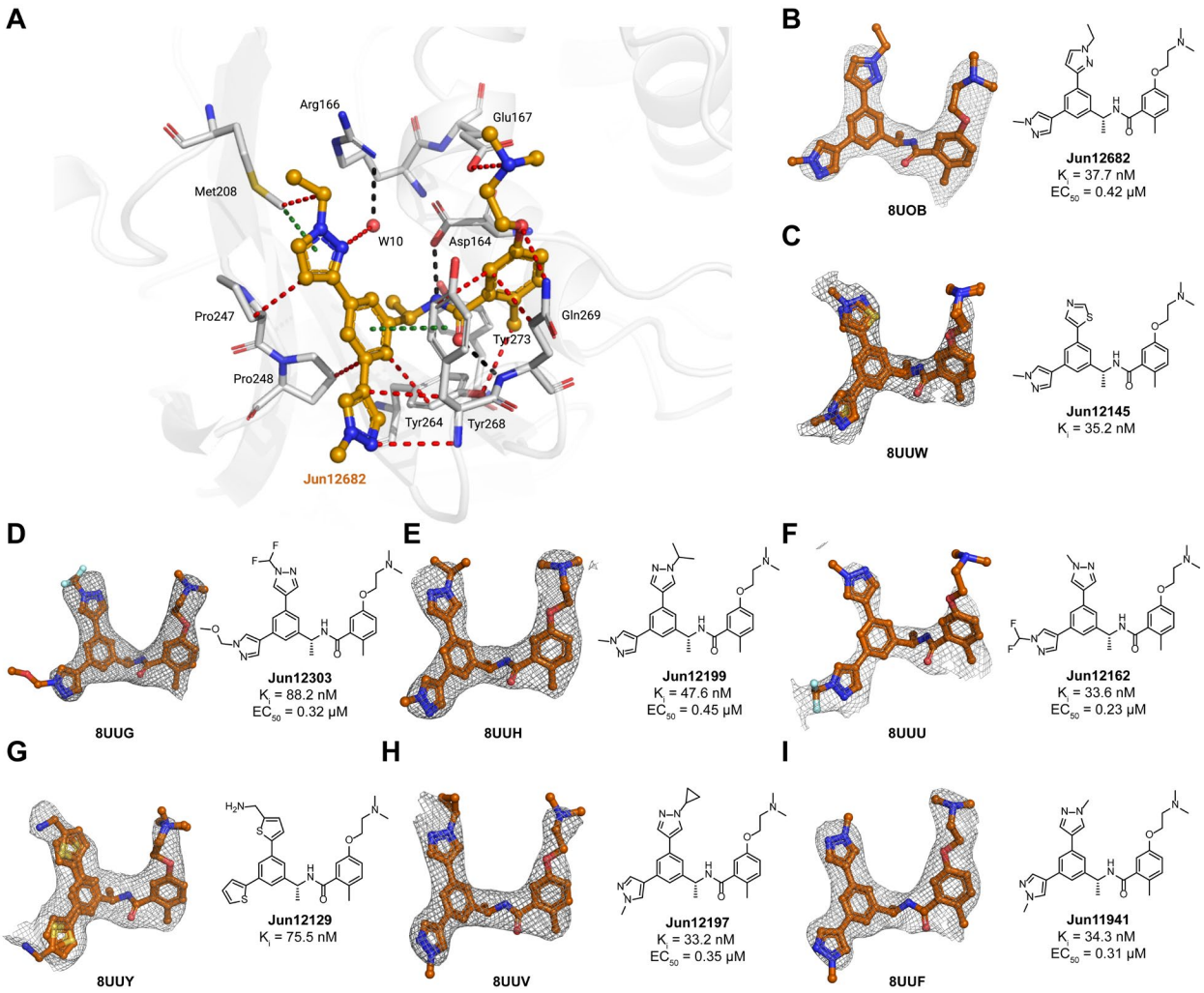

Fig. 3. X-ray crystal structures of SARS-CoV-2 PL^{pro} with biarylphenyl PL^{pro} inhibitors. (**A**) Atomic model of the **Jun12682** (in orange sticks and spheres) binding site in SARS-CoV-2 PL^{pro} (residues within 5 Å of the inhibitor are shown in light gray sticks), with hydrogen bonds displayed in black dashed lines, van der Waals contacts as red dashed lines, and π–π interactions as light green dashed lines. (**B-I**) Gallery of the polder maps of the indicated inhibitors, displayed as a grey mesh with contour levels between 2 and 4σ. The PL^{pro} inhibitory constant K_i in the FRET enzymatic assay and the SARS-CoV-2 antiviral activity EC_{50} in Caco-2 cells were shown for each compound.

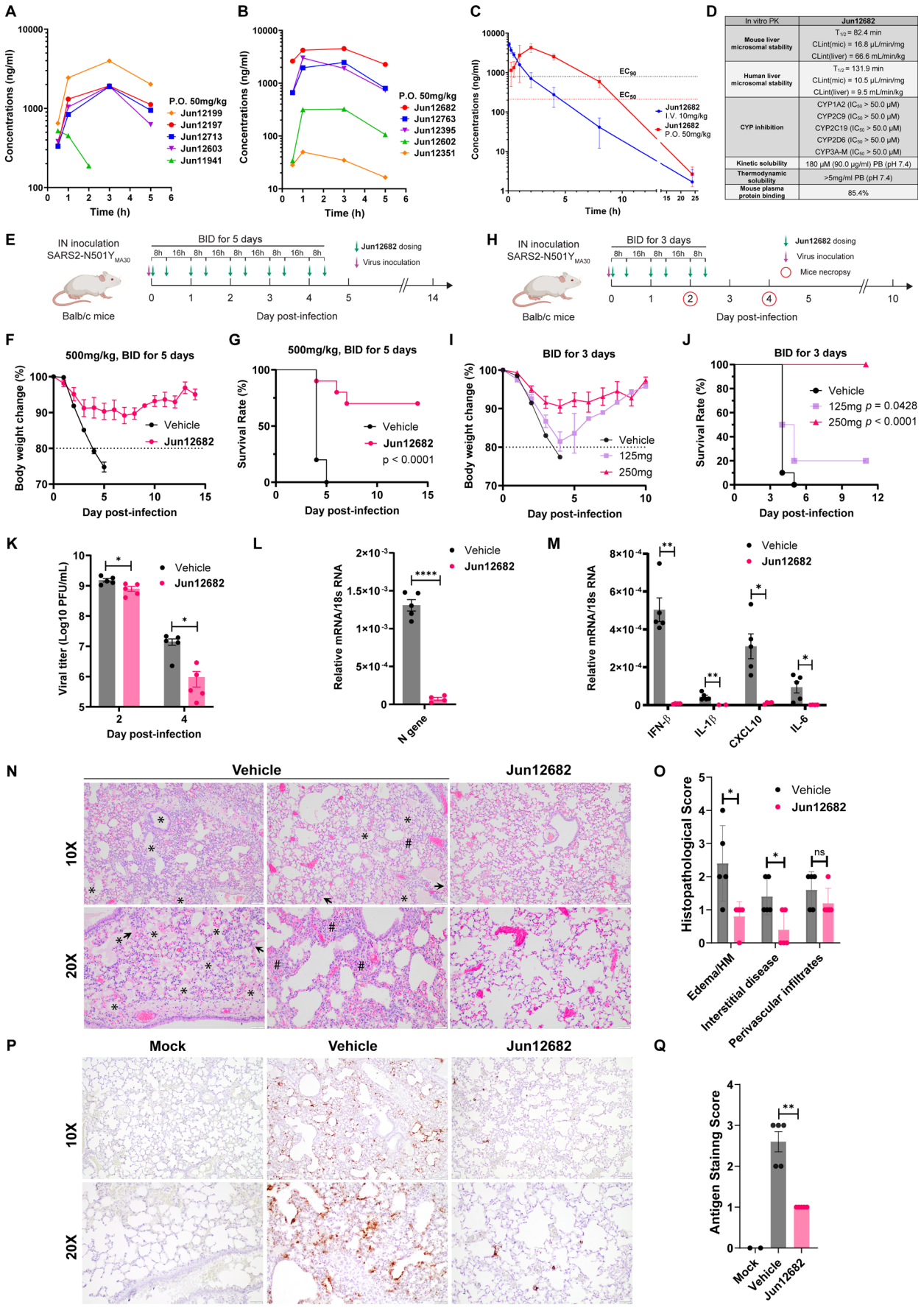

Fig. 4. *In vitro* and *in vivo* PK profiling of PL^{pro} inhibitors, and *in vivo* antiviral efficacy of Jun12682. (**A**) Plasma drug concentration of **Jun12199**, **Jun12197**, **Jun12713**, **Jun12603**, and **Jun11941** in C57BL/6J mice (6 – 8 weeks old) following p.o. administration of 50 mg/kg of compound in 0.5% methylcellulose and 2% Tween 80 in water. (**B**) Plasma drug concentration of **Jun12682**, **Jun12763**, **Jun12395**, **Jun12602**, and **Jun12351** in C57BL/6J mice (6 – 8 weeks old) following p.o. administration of 50 mg/kg of compound in 0.5% methylcellulose and 2% Tween 80 in water. (**C**) Plasma drug concentration of **Jun12682** in C57BL/6J mice (6 – 8 weeks old) following p.o. administration of 50 mg/kg and i.v. injection of 10 mg/kg. (**D**) *In vitro* PK parameters of **Jun12682**. (**E**) Experimental design for the 5-day treatment experiment. Ten mice per group were intranasally (IN) inoculated with 5,600 PFU of SARS2-N501Y$_{MA30}$ and subsequently orally administered 500 mg/kg **Jun12682** or vehicle twice a day (BID) for five days (BID_5). (**F**) Body weight loss and (**G**) survival rate of the BID_5 mice experiment. (**H**) Experimental design for the 3-day treatment experiment. Ten mice per group were intranasally (IN) inoculated with 5,600 PFU of SARS2-N501Y$_{MA30}$ and subsequently orally administered 125, 250 mg/kg **Jun12682** or vehicle BID for three days (BID_3). (**I**) Body weight loss and (**J**) survival rate of the BID_3 mice experiment. Data in **F**, **G**, **I**, and **J** are pool of two independent experiments (n=10) and are shown as mean ± s.e.m. The p values in **G** and **J** were determined using a log-rank (Mantel–Cox) test. (**K**) Viral titers in lungs collected at 2 and 4 DPI from vehicle- or 250 mg/kg **Jun12682**-treated mice (n=5 each group). Data are mean ± s.e.m and analyzed with unpaired t test with Welch's correction. *, p< 0.05; ***, p<0.001. (**L-M**) Quantitative PCR analysis of viral nucleocapsid gene (**L**) and cellular cytokines (**M**) in lungs collected at 2 DPI from vehicle- or 250mg/kg **Jun12682**-treated mice (n=5 each group). (**N-Q**) Lungs collected at 4 DPI from vehicle- or 250mg/kg **Jun12682**-treated mice (n=5 each group) were stained with haematoxylin and eosin (H&E) (**N**) or immunostained for SARS-CoV-2 nucleocapsid (**P**)**,** and the pathological lesions and staining were quantified (**O** and **Q**, respectively). **N**, H&E stained lungs from vehicle-treated infected mice exhibited airway edema (asterisks), hyaline membranes (HM, arrowheads), and interstitial thickness (number sign). Scale bars, 100 μm (top) and 50 μm (bottom). **O**, Summary scores of lung lesions (n = 5 for each group). **P**, Lungs from vehicle- or **Jun12682**-treated mice (n = 5 for each treatment group) were immunostained to detect SARS-CoV-2 nucleocapsid protein. Scale bars, 100 μm (top) and 50 μm (bottom). **Q**, Summary scores of nucleocapsid immunostaining of lungs. Data in **L, M, O** and **Q** are mean ± sem and analyzed with unpaired t test with Welch's correction. ns, not significant; *, p<0.05; **, p<0.01; ***, p<0.001; ****, p<0.0001.

Table 1. Representative biarylbenzamide series of SARS-CoV-2 PL^{pro} inhibitors.

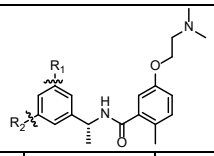

Compound ID	R_1	R_2	IC_{50} (nM)	K_i (nM)	CC_{50} (μM)	FlipGFP EC_{50} (μM)	Antiviral EC_{50} (μM)*	Microsomal Stability $T_{1/2}$ (min)	PDB code
Jun11875			66.2 ± 2.0	13.2 ± 2.0	4.5 ± 1.6	---	---	---	
Jun12129	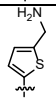		90.9 ± 4.6	75.5 ± 2.0	8.3 ± 1.2	---	---	---	8UUY
Jun12303	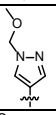		121.5 ± 4.0	88.2 ± 6.0	56.8 ± 7.4	2.6 ± 0.2	0.32	136	8UUG
Jun12763	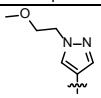		164.6 ± 23.0	37.2 ± 4.0	> 125	2.0 ± 0.3	0.96	---	
Jun12395			121.9 ± 8.0	47.1 ± 4.0	109.4 ± 16.2	2.9 ± 0.3	1.15	88.3	
Jun12713	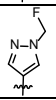		86.7 ± 6.0	34.0 ± 3.0	107.2 ± 6.2	2.7 ± 0.6	0.86	---	
Jun12602	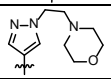		116.7 ± 9.2	46.9 ± 3.0	> 125	14.7 ± 2.5	0.80	> 145	
Jun11941			151.4 ± 4.0	34.3 ± 3.0	54.8 ± 8.3	1.8 ± 0.2	0.31	> 145	8UUF
Jun12162	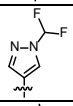		98.3 ± 7.0	33.6 ± 3.0	42.3 ± 2.3	2.1 ± 0.2	0.23	76.7	8UUU
Jun12199			108.8 ± 10.2	47.6 ± 3.0	63.2 ± 11.3	0.8 ± 0.1	0.45	79.7	8UUH
Jun12197			102.7 ± 10.2	33.2 ± 3.0	43.7 ± 5.1	0.6 ± 0.1	0.35	116.0	8UUV
Jun12351	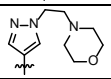		98.8 ± 5.2	29.3 ± 3.0	> 125	2.0 ± 0.4	0.59	> 145	
Jun12603			112.2 ± 6.0	39.8 ± 4.0	61.0 ± 19.3	2.4 ± 0.4	0.50	---	
Jun12145			108.5 ± 6.2	35.2 ± 2.0	31.3 ± 5.4	1.3 ± 0.3	0.58	26.3	8UUW
Jun12682			106.8 ± 5.0	37.7 ± 3.0	61.3 ± 4.5	1.1 ± 0.1	0.42	82.4	8UOB
GRL0617	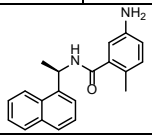		1918.0 ± 150.0	1374 ± 58	107.3 ± 10.9	22.4 ± 2.3	> 20	---	7JRN

*The positive control nirmatrelvir had an EC_{50} of 0.04 μM in the SARS-CoV-2 antiviral assay.

References and notes

1. G. Li, R. Hilgenfeld, R. Whitley, E. De Clercq, Therapeutic strategies for COVID-19: progress and lessons learned. *Nat Rev Drug Discov* **22**, 449-475 (2023).
2. W. H. O. S. T. Consortium, Remdesivir and three other drugs for hospitalised patients with COVID-19: final results of the WHO Solidarity randomised trial and updated meta-analyses. *Lancet* **399**, 1941-1953 (2022).
3. L. D. Saravolatz, S. Depcinski, M. Sharma, Molnupiravir and Nirmatrelvir-Ritonavir: Oral Coronavirus Disease 2019 Antiviral Drugs. *Clin Infect Dis* **76**, 165-171 (2023).
4. D. R. Owen *et al.*, An oral SARS-CoV-2 M(pro) inhibitor clinical candidate for the treatment of COVID-19. *Science* **374**, 1586-1593 (2021).
5. Y. Unoh *et al.*, Discovery of S-217622, a Noncovalent Oral SARS-CoV-2 3CL Protease Inhibitor Clinical Candidate for Treating COVID-19. *J Med Chem* **65**, 6499-6512 (2022).
6. H. Mukae *et al.*, Efficacy and Safety of Ensitrelvir in Patients With Mild-to-Moderate Coronavirus Disease 2019: The Phase 2b Part of a Randomized, Placebo-Controlled, Phase 2/3 Study. *Clin Infect Dis* **76**, 1403-1411 (2023).
7. R. Shimizu *et al.*, Evaluation of the Drug-Drug Interaction Potential of Ensitrelvir Fumaric Acid with Cytochrome P450 3A Substrates in Healthy Japanese Adults. *Clin Drug Investig* **43**, 335-346 (2023).
8. R. Shimizu *et al.*, Safety, Tolerability, and Pharmacokinetics of the Novel Antiviral Agent Ensitrelvir Fumaric Acid, a SARS-CoV-2 3CL Protease Inhibitor, in Healthy Adults. *Antimicrob Agents Chemother* **66**, e0063222 (2022).
9. S. Iketani *et al.*, Multiple pathways for SARS-CoV-2 resistance to nirmatrelvir. *Nature* **613**, 558-564 (2023).
10. Y. Hu *et al.*, Naturally Occurring Mutations of SARS-CoV-2 Main Protease Confer Drug Resistance to Nirmatrelvir. *ACS Cent Sci* **9**, 1658-1669 (2023).
11. L. J. Stevens *et al.*, Mutations in the SARS-CoV-2 RNA-dependent RNA polymerase confer resistance to remdesivir by distinct mechanisms. *Sci Transl Med* **14**, eabo0718 (2022).
12. S. Gandhi *et al.*, De novo emergence of a remdesivir resistance mutation during treatment of persistent SARS-CoV-2 infection in an immunocompromised patient: a case report. *Nat Commun* **13**, 1547 (2022).
13. N. S. Zuckerman, E. Bucris, D. Keidar-Friedman, M. Amsalem, T. Brosh-Nissimov, Nirmatrelvir resistance - de novo E166V/L50V mutations in an immunocompromised patient treated with prolonged nirmatrelvir/ritonavir monotherapy leading to clinical and virological treatment failure - a case report. *Clin Infect Dis* doi: 10.1093/cid/ciad494, (2023).
14. C. P. Sjaarda *et al.*, Prevalence of Low-Frequency, Antiviral Resistance Variants in SARS-CoV-2 Isolates in Ontario, Canada, 2020-2023. *JAMA Netw Open* **6**, e2324963 (2023).
15. Y. Hirotsu *et al.*, Multidrug-resistant mutations to antiviral and antibody therapy in an immunocompromised patient infected with SARS-CoV-2. *Med* **4**, 813-824.e4 (2023).
16. W. Rut *et al.*, Activity profiling and crystal structures of inhibitor-bound SARS-CoV-2 papain-like protease: A framework for anti-COVID-19 drug design. *Sci Adv* **6**, eabd4596 (2020).
17. D. Shin *et al.*, Papain-like protease regulates SARS-CoV-2 viral spread and innate immunity. *Nature* **587**, 657-662 (2020).

18. P. M. Wydorski *et al.*, Dual domain recognition determines SARS-CoV-2 PLpro selectivity for human ISG15 and K48-linked di-ubiquitin. *Nat Commun* **14**, 2366 (2023).
19. Y. M. Baez-Santos, S. E. St John, A. D. Mesecar, The SARS-coronavirus papain-like protease: structure, function and inhibition by designed antiviral compounds. *Antiviral Res* **115**, 21-38 (2015).
20. H. Tan, Y. Hu, P. Jadhav, B. Tan, J. Wang, Progress and Challenges in Targeting the SARS-CoV-2 Papain-like Protease. *J Med Chem* **65**, 7561-7580 (2022).
21. J. Lei, Y. Kusov, R. Hilgenfeld, Nsp3 of coronaviruses: Structures and functions of a large multi-domain protein. *Antiviral Res* **149**, 58-74 (2018).
22. C. Ma *et al.*, Discovery of SARS-CoV-2 Papain-like Protease Inhibitors through a Combination of High-Throughput Screening and a FlipGFP-Based Reporter Assay. *ACS Cent Sci* **7**, 1245-1260 (2021).
23. A. K. Ghosh, J. L. Mishevich, A. Mesecar, H. Mitsuya, Recent Drug Development and Medicinal Chemistry Approaches for the Treatment of SARS-CoV-2 Infection and COVID-19. *ChemMedChem* **17**, e202200440 (2022).
24. Z. Shen *et al.*, Design of SARS-CoV-2 PLpro Inhibitors for COVID-19 Antiviral Therapy Leveraging Binding Cooperativity. *J Med Chem* **65**, 2940-2955 (2022).
25. B. C. Sanders *et al.*, Potent and selective covalent inhibition of the papain-like protease from SARS-CoV-2. *Nat Commun* **14**, 1733 (2023).
26. G. Platzer *et al.*, PI by NMR: Probing CH-π Interactions in Protein-Ligand Complexes by NMR Spectroscopy. *Angewandte Chemie* **59**, 14861-14868 (2020).
27. B. R. Beno, K. S. Yeung, M. D. Bartberger, L. D. Pennington, N. A. Meanwell, A Survey of the Role of Noncovalent Sulfur Interactions in Drug Design. *J Med Chem* **58**, 4383-4438 (2015).
28. H. Tan, Y. Hu, J. Wang, FlipGFP protease assay for evaluating in vitro inhibitory activity against SARS-CoV-2 M(pro) and PL(pro). *STAR Protoc* **4**, 102323 (2023).
29. T. Klemm *et al.*, Mechanism and inhibition of the papain-like protease, PLpro, of SARS-CoV-2. *EMBO J* **39**, e106275 (2020).
30. L. R. Wong *et al.*, Eicosanoid signalling blockade protects middle-aged mice from severe COVID-19. *Nature* **605**, 146-151 (2022).
31. S. A. El-Kafrawy *et al.*, SARS-CoV-2-specific immunoglobulin Y antibodies are protective in infected mice. *PLoS Pathog* **18**, e1010782 (2022).
32. L. Zhang *et al.*, Viral anti-inflammatory serpin reduces immuno-coagulopathic pathology in SARS-CoV-2 mouse models of infection. *EMBO Mol Med* **15**, e17376 (2023).
33. J. Shi *et al.*, RBD-mRNA vaccine induces broadly neutralizing antibodies against Omicron and multiple other variants and protects mice from SARS-CoV-2 challenge. *Transl Res* **248**, 11-21 (2022).
34. V. Fumagalli *et al.*, Nirmatrelvir treatment of SARS-CoV-2-infected mice blunts antiviral adaptive immune responses. *EMBO Mol Med* **15**, e17580 (2023).
35. H. Nobori *et al.*, Efficacy of ensitrelvir against SARS-CoV-2 in a delayed-treatment mouse model. *J Antimicrob Chemother* **77**, 2984-2991 (2022).
36. D. Liebschner *et al.*, Polder maps: improving OMIT maps by excluding bulk solvent. *Acta Crystallogr D Struct Biol* **73**, 148-157 (2017).